

Stiffness tuning of FeGa structures manufactured by Ultrasonic Additive Manufacturing

Justin J. Scheidler, Marcelo J. Dapino

Smart Vehicle Concepts Center, Department of Mechanical and Aerospace Engineering,
The Ohio State University, Columbus, OH, USA, 43210

ABSTRACT

This paper investigates the use of Galfenol (FeGa) composite beams as solid-state, adaptive vibration absorbers that have an electrically-tunable stiffness. The study encompasses the manufacture of these structures by ultrasonic additive manufacturing (UAM) and the formulation of a continuous model for the beams' bending vibrations. The beams' 1st and 3rd resonant frequencies are calculated as a function of base acceleration, Galfenol volume fraction, and DC magnetic field. The effects of an axial force, viscoelastic material damping, beam nonuniformity, and Galfenol's nonlinear behavior are incorporated. Autoresonant feedback control is used as a numerical technique to maintain the resonant state under changes in the inputs. The model is validated by comparing (1) calculated and analytical frequency responses and (2) calculated and measured resonant frequencies and modes shapes of a Galfenol/Al 6061 composite beam that was manufactured using UAM. The modeling results show that by varying the DC magnetic field, the resonant frequency can be tuned between 3 % and 51 % for Galfenol/Al 6061 composites containing from 10 % to 100 % Galfenol by volume, respectively. The magnitude of this change will increase for composites that have a softer matrix. The axial force was found to have only a small effect on the maximum resonant frequency tunability, but, for high Galfenol volume fractions, was also found to broaden the region over which tuning can occur.

Keywords: ultrasonic additive manufacturing, Galfenol, adaptive vibration absorber, autoresonant feedback control, stiffness tuning

1. INTRODUCTION

Vibration absorbers are a common solution when undesirable vibration or transmitted forces cannot be reduced through direct design modifications (e.g., by introducing additional damping or shifting natural frequencies away from operating conditions). While conventional absorbers must be designed for a specific operating condition and vibrating structure, adaptive vibration absorbers (AVAs) can tune their response in conjunction with changes in operating conditions. A number of smart materials can provide a compact, solid-state source of stiffness change. Piezoelectric, magnetorheological, and magnetostrictive materials have been investigated.^{1,2}

Key factors in the selection of an active material for AVAs include the tunability of the material's resonant frequency, its durability, and its mechanism for generating stiffness changes. Considering these factors, Galfenol ($\text{Fe}_{100-x}\text{Ga}_x$, $13 \leq x \leq 29$ at %) is an attractive material due to its non-contact, high speed operation, ~ 500 MPa tensile strength,³ and ability to increase its elastic modulus 160% above a baseline value,⁴ which is comparable to Terfenol-D (161%)⁵ and PZT (155%).^{6,7} This elastic modulus change is a direct result of the magnetoelastic coupling in the material. As Galfenol is stressed from a demagnetized state, both purely elastic and magnetoelastic strain occur as the magnetic state of the material changes, thereby reducing the material's effective elastic modulus relative to the magnetically-saturated state.

Recent advancements in manufacturing technology have enabled the development of composites containing active materials. By harnessing Galfenol's robustness and its electrically-tunable elastic modulus,

Further author information: (Send correspondence to M.J.D)
J.J.S.: E-mail: scheidler.8@osu.edu, Telephone: 1-614-247-7480
M.J.D.: E-mail: dapino.1@osu.edu, Telephone: 1-614-688-3689

load-bearing composites that provide a controllable stiffness can be realized. One enabling technology is ultrasonic additive manufacturing (UAM), a metal layering technique for creating multimaterial composites containing seamlessly-embedded smart materials. UAM is a low temperature rapid prototyping process based on solid-state welding of metal foils to themselves or to a metallic substrate. In UAM, a sonotrode applies transverse ultrasonic vibration (>20 kHz) to the tape-substrate pair creating a scrubbing action that shears asperities and disperses surface contaminants and oxides. The resulting nascent surfaces metallurgically bond under an applied normal force. A 9 kW UAM machine and a schematic of the ultrasonic weld head are shown in Figure 1. Metallic tapes are welded additively to form bulk 3D geometries, which may include complex internal channels created through periodic machining.

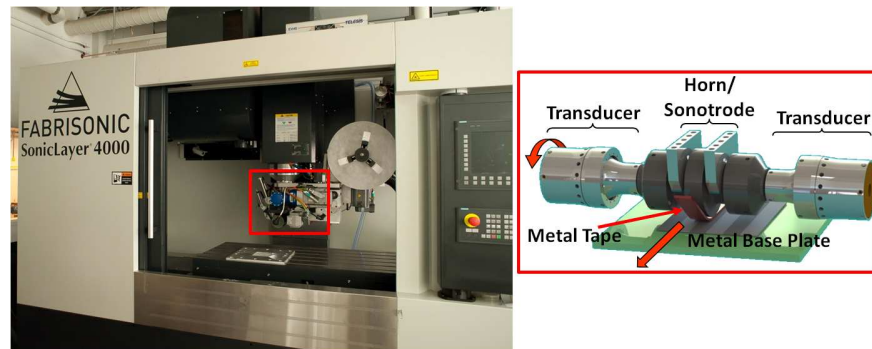


Figure 1. Very high power UAM machine installed in the Center for Ultrasonic Additive Manufacturing at The Ohio State University, and schematic of the ultrasonic system (motion during welding shown by arrows).

The manufacture of layered structures by UAM is computer controlled and automatic. A tape feed mechanism supplies the metal foils to the weld head and cuts them at the beginning and end of each pass. Embedding smart materials is presently done by combining this automatic process for layering of the matrix along with manual placement of the smart materials. Galfenol is best embedded as sheet stock or wires. Depending on the thickness of the Galfenol features relative to the typical foil thickness (0.15 mm or 0.006 in), grooves are machined in the matrix to partially bury the material under the surface of the build. This is done via the built-in CNC mill or laser etching system.

The use of Galfenol for stiffness tuning applications was previously investigated by Datta et al.,⁴ who measured and modeled material-level changes in Galfenol's elastic modulus in response to stress and magnetic field inputs. Scheidler and Dapino^{8,9} calculated, using a lumped parameter approach, the resonant frequency tunability of a composite beam containing Galfenol. Clamped-clamped and clamped-free boundary conditions were considered, but the effect of an axial force was neglected. For nonlinear systems that do not permit the formulation of an eigenvalue problem, the conventional approach for calculating resonant frequencies is to approximate the nonlinear frequency response using a large number of time domain simulations. This approach, which is computationally intensive, especially for multi-degree-of-freedom systems, was used by Scheidler and Dapino.^{8,9} In this paper, the resonant frequency of the continuous beam is efficiently calculated numerically with autoresonant feedback control.

Autoresonant feedback control was born from the study of vibro-impact systems, which operate near resonance.¹⁰ In high quality factor (Q-factor) systems, resonance is very sensitive to changes in the system's parameters and inputs, and occurs at the boundary of stability for some linear systems and for frequency-controlled excitation of nonlinear systems. Autoresonant feedback control resolves these limitations by exciting the system with a vibration signal that is shifted by the resonant phase ϕ^* to automatically reach and maintain resonance under changes in natural frequency. Sokolov and Babitsky¹¹ detailed the characteristics of single- and two-degree-of-freedom autoresonant systems, showing the flatness and single-valuedness of the amplitude versus phase curves that govern phase-controlled systems. Autoresonant feedback control has been utilized in various applications, but primarily for ultrasonically-assisted machining.¹² Recently,

Twiefel¹³ applied autoresonant feedback control numerically to efficiently conduct parametric studies on the mode shape of a piezoelectric beam.

The objective of this paper is to characterize and model Galfenol composite beams as AVAs that are subjected to axial loads and operate at an arbitrary mode of the beam. These composites can be effectively manufactured using UAM. In this paper, the characterization is performed by calculating the beam's resonant frequency as a function of (a) mode number, (b) base acceleration magnitude, (c) DC magnetic field, and (d) Galfenol volume fraction. Resonant frequencies are calculated from time domain responses by incorporating autoresonant feedback control. The continuous, nonlinear bending vibration of the composite beams is modeled using Euler-Bernoulli beam theory. The effects of axial force on the beam, viscoelastic material damping, and beam nonuniformity are included. The constitutive behavior of Galfenol is modeled by a fully-coupled, nonlinear model that was first developed by Evans and Dapino.¹⁴ The distributed parameter model is spatially discretized using the finite difference method. The resulting state-space system is then implemented in Simulink and solved using the Runge-Kutta-Fehlberg method. The model is validated by comparing numerical frequency domain responses to analytical responses, which are derived for the case of a passive beam. Further validation is presented by comparing calculated and measured resonant frequencies and mode shapes of a UAM composite beam containing Galfenol.

2. MODEL DEVELOPMENT

The system of interest is a metal-matrix composite beam composed of a single matrix material and a single sheet of Galfenol. The system and finite difference nodes are shown in Figure 2. The beam's cross section and an example Galfenol/Al 6061 composite manufactured using UAM are shown in Figure 3.

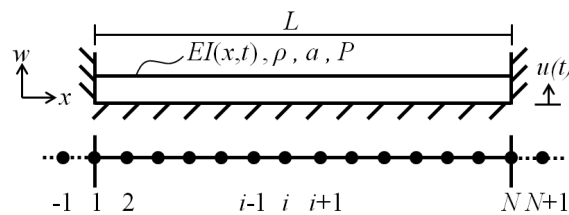


Figure 2. Schematic of the base-excited magnetostrictive composite beam and nodes used for finite difference discretization.

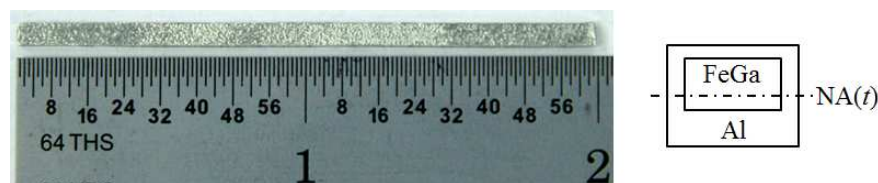


Figure 3. Galfenol/Al 6061 composite beam manufactured using UAM and schematic of the beam's cross section; Galfenol and composite dimensions (thickness x width) are 0.51 x 1.02 and 1.02 x 1.91 mm, respectively.

To investigate the effect of an axial force on the dynamic behavior of this composite, clamped-clamped (C-C) boundary conditions are considered. In order to characterize the beam's suitability for use as an AVA, a distributed parameter model of the beam's transverse vibration is presented. To incorporate the nonlinearity resulting from Galfenol's stress- and magnetic field-dependent elastic modulus, the nonuniformity of the beam along its length is fully retained. The nonuniformity through the thickness is approximated following results by Scheidler and Dapino.⁹ AVAs are implemented by coupling them to a host structure exhibiting undesirable vibration. As such, the response of the beam to base excitation is modeled.

Material damping in the composite is modeled as viscoelastic, which is frequency dependent. This model was selected over hysteretic damping, which is frequency independent, because it is well known that

ferromagnetic materials exhibit frequency-dependent hysteresis due to eddy currents, which occur even for stress application in the absence of AC magnetic fields. In this paper, the Kelvin-Voigt model for viscoelastic material damping is adopted. This damping model was successfully used (in a simplified form) for the modeling of Galfenol unimorphs by Shu et al.¹⁵ The following assumptions are used to develop the proposed model detailed in the subsequent sub-sections:

- Euler-Bernoulli beam theory (i.e., small deflections and negligible shear deformation)
- Mass per unit length of the beam ρA and Kelvin-Voigt damping constant a are constant and uniform
- Bias magnetic field H is uniform
- The uniform axial force P is calculated from a static analysis of the 1-D composite

2.1 Beam vibration model

In this sub-section, the state-space system is derived by discretizing the PDE governing transverse vibration of the composite beam. The axial force is then derived, after which the flexural rigidity is presented in the context of unidirectional composites. From Meirovitch,¹⁶ the governing equation for the transverse vibration of the Euler-Bernoulli beam considered above is

$$\rho A \ddot{w}(x, t) + [EI(x, t) (a \dot{w}_{xx}(x, t) + w_{xx}(x, t))]_{xx} - P(t) w_{xx}(x, t) = f(x, t), \quad (1)$$

where P is the uniform axial force, f denotes the applied distributed force, ρ and A are the density and cross-sectional area, respectively, EI represents the flexural rigidity, a is a viscoelastic parameter for the Kelvin-Voigt damping model, w is the transverse deflection of the beam, and w_x and \dot{w} denote partial derivatives of w with respect to x and t , respectively; EI is state-dependent and nonuniform. For base excitation, the total deflection is written as

$$w(x, t) = \bar{w}(x, t) + u(t), \quad (2)$$

where $\bar{w}(x, t)$ is the beam's displacement relative to the base and u is the base displacement. Insertion of (2) into (1) and neglecting the applied force gives

$$\rho A \ddot{\bar{w}}(x, t) + [EI(x, t) (a \dot{\bar{w}}_{xx}(x, t) + \bar{w}_{xx}(x, t))]_{xx} - P(t) \bar{w}_{xx}(x, t) = -\rho A \ddot{u}(t). \quad (3)$$

Thus, in terms of the relative displacement $\bar{w}(x, t)$, the base-excited system can be viewed as a beam with static boundary conditions subject to an equivalent force,

$$f_{eq}(t) = -\rho A \ddot{u}(t). \quad (4)$$

After expanding the differentiation, (3) can be written as

$$\rho A \ddot{\bar{w}}(x, t) + F^C(\dot{\bar{w}}, t) + F^K(\bar{w}, t) = f_{eq}(t), \quad (5)$$

where the damping force F^C is

$$F^C(\dot{\bar{w}}, t) = a (EI_{xx} \dot{\bar{w}}_{xx} + 2EI_x \dot{\bar{w}}_{xxx} + EI \dot{\bar{w}}_{xxxx}), \quad (6)$$

and the flexural force F^K is

$$F^K(\bar{w}, t) = EI_{xx} \bar{w}_{xx} + 2EI_x \bar{w}_{xxx} + EI \bar{w}_{xxxx} - P \bar{w}_{xx}. \quad (7)$$

The governing PDE given by (5) - (7) does not admit an eigenvalue problem nor a closed-form solution due to the beam's spatial and temporal nonuniformity, which results from the magnetic field- and stress-dependent elastic properties of the Galfenol component. Consequently, the PDE is solved approximately by

(i) discretizing the beam (Fig. 2), (ii) using the finite difference method to approximate spatial derivatives and express the discretized system in state-space form, and (iii) using the explicit Runge-Kutta-Fehlberg method (MATLAB's *ode45*) to solve the state-space system iteratively.

Following discretization, the continuous PDE (5) becomes a system of discrete PDEs in terms of the unknown nodal displacements \bar{w}_i and their derivatives, where $i = 2, \dots, N-1$ since the boundary conditions provide $\bar{w}_1 = \bar{w}_N = \bar{w}_{x_1} = \bar{w}_{x_N} = 0$. Of the standard finite difference methods (backward, central, and forward), the central difference method provides the best accuracy;¹⁷ however, it may be undefined at or near boundaries due to its dependence on fictitious nodes $i = -1, -2, \dots$ or $i = N+1, N+2, \dots$.

Using the 2nd order central difference method¹⁷ to approximate the spatial partial derivatives, (6) and (7) can be written at the i^{th} node as

$$F_i^C(t) \approx a\Delta x^{-4} (A_i \dot{w}_{i+2} + B_i \dot{w}_{i+1} + C_i \dot{w}_i + D_i \dot{w}_{i-1} + G_i \dot{w}_{i-2}), \quad (8)$$

and

$$\begin{aligned} F_i^K(t) &\approx \Delta x^{-4} (A_i \bar{w}_{i+2} + (B_i - \bar{P}) \bar{w}_{i+1} + (C_i + 2\bar{P}) \bar{w}_i + (D_i - \bar{P}) \bar{w}_{i-1} + G_i \bar{w}_{i-2}) \\ &= \Delta x^{-4} (\bar{A}_i \bar{w}_{i+2} + \bar{B}_i \bar{w}_{i+1} + \bar{C}_i \bar{w}_i + \bar{D}_i \bar{w}_{i-1} + G_i \bar{w}_{i-2}), \end{aligned} \quad (9)$$

where

$$\begin{aligned} \bar{P} &= \Delta x^2 P \\ A_i &= EI_i + \frac{1}{2}(EI_{i+1} - EI_{i-1}) \\ B_i &= -6EI_i + 2EI_{i-1} \\ C_i &= -2EI_{i+1} + 10EI_i - 2EI_{i-1} \\ D_i &= -6EI_i + 2EI_{i+1} \\ G_i &= EI_i - \frac{1}{2}(EI_{i+1} - EI_{i-1}). \end{aligned} \quad (10)$$

Evaluation of (8) and (9) at nodes $i = 2$ and $i = N-1$ therefore depends on the fictitious nodes \bar{w}_{-1} and \bar{w}_{N+1} , respectively. However, by approximating the boundary condition on the slope of the beam using the 2nd order central difference method, the following relations can be derived:

$$\bar{w}_{-1} \approx \bar{w}_2, \quad \bar{w}_{N+1} \approx \bar{w}_{N-1}. \quad (11)$$

Using the relations (11), the 2nd order central difference approximation of the damping force F_i^C and flexural force F_i^K can be evaluated at all interior nodes.

Since the approximate damping and flexural forces depend only on the nodal velocities and displacements, respectively, the set of $(N-2)$ discrete PDEs approximating (5) - (7) can be written in a form resembling a standard multi-degree-of-freedom system,

$$[M] \{\ddot{\bar{w}}\} + [\bar{C}] \{\dot{\bar{w}}\} + [\bar{K}] \{\bar{w}\} = \{f_{eq}\}, \quad (12)$$

where n denotes the order of the error in the approximation of the damping and flexural forces. When the beam is free from an added mass, the global mass matrix $[M]$ is

$$[M] = \rho A [I], \quad (13)$$

where $[I]$ is the identity matrix. Added masses can be incorporated by increasing ρA at nodes over which the mass is located. For this case, $[M]$ remains diagonal. The 2nd order accurate damping and stiffness matrices ($[\bar{C}]$ and $[\bar{K}]$) are pentadiagonal matrices, as detailed in Appendix A. If increased accuracy is necessary,

$^4[C]$ and $^4[K]$ may be derived using the 4th order central difference method, as shown in Appendix A. For this case, the damping and stiffness matrices are heptadiagonal. Consequently, the system matrices can be considered sparse when a reasonable number of nodes is used. By defining the state vector W as the nodal displacements and velocities, the state-space representation of (12) can be written as

$$\dot{W} = \begin{bmatrix} [0] & [I] \\ -[M]^{-1}[K] & -[M]^{-1}[C] \end{bmatrix} \begin{Bmatrix} \{\bar{w}\} \\ \{\dot{\bar{w}}\} \end{Bmatrix} + \begin{Bmatrix} \{0\} \\ [M]^{-1}\{f_{eq}\} \end{Bmatrix}. \quad (14)$$

The state-space system is implemented and solved in Simulink to utilize an available solver and to improve computational efficiency by precompiling the model.

2.1.1 Calculation of the axial force P

The application of a magnetic field to the composite generates magnetostriction λ in the Galfenol element that is counteracted by the matrix and by a compressive force due to the fixed boundary conditions. To derive an expression for the axial force that develops in the composite, static analysis of a free-free composite subjected to a magnetic field is first considered (Figure 4a).

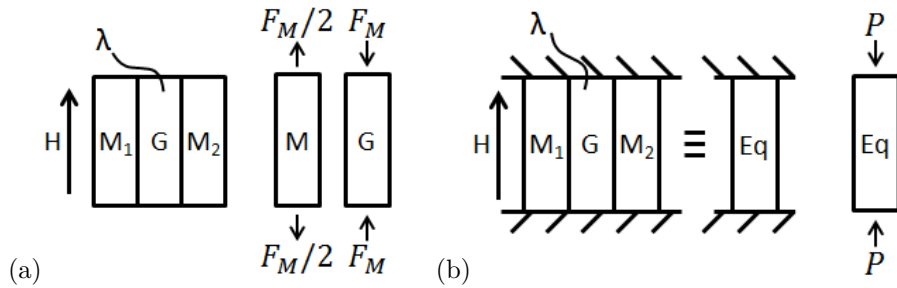


Figure 4. Schematic and free body diagram of the 1-D static composite subjected to an applied magnetic field with boundary conditions: (a) free-free, and (b) fixed-fixed.

Free body diagrams of the matrix and Galfenol constituents are given in Figure 4a, assuming that a uniform shear stress acts between Galfenol and the surrounding matrix. Further assuming that there is no slip at the interfaces, the displacement compatibility between the layers can be expressed as

$$\begin{aligned} \delta_{F-F} &= \delta_G = \delta_{M_1} = \delta_{M_2} \\ &= \frac{-F_M L}{A_G E_G} + \lambda L = \frac{(F_M/2)L}{A_M E_M}, \end{aligned} \quad (15)$$

where δ_{F-F} , δ_G , and δ_{M_1} are the displacements of the free-free composite, the Galfenol section, and one of the matrix sections; E_M and E_G are the elastic moduli of the matrix and Galfenol, respectively; and A_M and A_G are the cross-sectional areas of one of the matrix sections and the Galfenol section, respectively. Rearranging (15) one gets the total force on the Galfenol section applied by the matrix,

$$F_M = \frac{2\lambda(A_M E_M)(A_G E_G)}{A_G E_G + 2A_M E_M}. \quad (16)$$

Insertion of (16) in (15) gives the free-free deflection,

$$\delta_{F-F} = \delta_G = \lambda \left(1 - \frac{2A_M E_M}{A_G E_G + 2A_M E_M}\right) L = \lambda_{eff} L, \quad (17)$$

where λ_{eff} is the effective magnetostriction of the composite. The effective magnetostriction is consistent with the cases of no matrix ($A_M = 0$) and no Galfenol ($A_G = 0$), for which the magnetostriction in the composite is λ and 0, respectively. Now consider a static, fixed-fixed composite and its homogeneous

equivalent (Figure 4b). By writing a compatibility equation for the equivalent beam, the axial force on the composite can be written as

$$P = -\lambda_{\text{eff}} A_{\text{eq}} E_{\text{eq}}, \quad (18)$$

where the parameters of the equivalent beam are found by considering the matrix and Galfenol as springs in parallel,

$$A_{\text{eq}} E_{\text{eq}} = A_{\text{G}} E_{\text{G}} + 2A_{\text{M}} E_{\text{M}}. \quad (19)$$

2.1.2 Calculation of the flexural rigidity EI_i

Solution of the state-space system (14) requires calculation of the flexural rigidity EI_i at each time step for all nodes. The composite's area moment of inertia I_i is a function of the cross-sectional geometry of an equivalent, homogeneous cross section of Galfenol, which depends upon the elastic moduli of the matrix E_i^{M} and Galfenol $E_i^{\text{G}}(x, t)$. The elastic modulus E_i of a unidirectional composite is found using the rule of mixtures given by Agarwal et al.,¹⁸

$$E_i(x, t) = E_i^{\text{M}} V^{\text{M}} + E_i^{\text{G}}(x, t) V^{\text{G}}, \quad (20)$$

where V^{M} and V^{G} denote the matrix and Galfenol volume fractions, respectively. Consequently, a constitutive model for Galfenol is needed to calculate the magnetic field- and stress-dependent flexural rigidity of the composite. As detailed in ref.,⁹ before calculating the elastic modulus in the Galfenol element, the stress must be calculated using an inverse of the constitutive model, which has inputs of magnetic field and strain. In this paper, the strain in the beam is calculated using the exact expression for an Euler-Bernoulli beam,

$$S = -y \bar{w}_{xx} (1 + \bar{w}_x^2)^{-3/2}. \quad (21)$$

The spatial derivatives in (21) are calculated at interior nodes $i = 3, \dots, N - 2$ using the 4th order central difference method. The 2nd order backward, central, and forward difference methods are used for the remaining nodes.

This work utilizes a fully-coupled, nonlinear energy-averaged model for cubic magnetostrictive materials developed by Evans and Dapino,¹⁴ which is accurate yet efficient and has been successfully used for the modeling of Galfenol-based systems of varying dimensionality.^{15, 19-21} This model is summarized in the following sub-section.

2.2 FeGa constitutive model review

The Evans and Dapino (ED) model¹⁴ describes Galfenol as a collection of non-interacting, mesoscopic magnetic domains. While earlier energy-averaged models consider a large number of possible magnetic domain orientations that are fixed, the ED model maintains accuracy while significantly improving computational efficiency by considering only 6 possible directions that rotate in response to the inputs – magnetic field \mathbf{H} and stress \mathbf{T} . The 6 possible magnetic domain orientations \mathbf{m}^k are calculated by minimizing an energy function that is locally-defined about each of the 6 easy crystallographic directions, subject to the constraint $\|\mathbf{m}^k\| = 1$. The total free energy G of a magnetic moment in the vicinity of the k^{th} easy direction \mathbf{c}^k incorporates the local magnetocrystalline (anisotropy)*, magnetoelastic (magnetomechanical coupling), and magnetic field (Zeeman) energies, and can be written in matrix form as

$$G = \frac{1}{2} \mathbf{m}^k \cdot \mathbf{K} \mathbf{m}^k - \mathbf{m}^k \cdot \mathbf{B} + K_0, \quad k = \pm 1, \pm 2, \pm 3, \quad (22)$$

*The improved anisotropy energy given by Chakrabarti²² is used.

where K and K_0^k are anisotropy energy constants, M_s is the saturation magnetization, λ_{100} and λ_{111} are magnetostriction constants, and

$$\mathbf{K} = \begin{bmatrix} K - 3\lambda_{100}T_{xx} & -3\lambda_{111}T_{xy} & -3\lambda_{111}T_{xz} \\ -3\lambda_{111}T_{xy} & K - 3\lambda_{100}T_{yy} & -3\lambda_{111}T_{yz} \\ -3\lambda_{111}T_{xz} & -3\lambda_{111}T_{yz} & K - 3\lambda_{100}T_{zz} \end{bmatrix}, \quad (23)$$

$$\mathbf{B}^k = \begin{bmatrix} c_1^k K + \mu_o M_s H_x & c_2^k K + \mu_o M_s H_y & c_3^k K + \mu_o M_s H_z \end{bmatrix}^T. \quad (24)$$

By linearizing the constraint about \mathbf{c}^k and using the Lagrange multipliers method, Evans and Dapino¹⁴ found an explicit solution that approximately minimizes the energy (22). Recently, Tari et al.²³ derived the exact solution,

$$\mathbf{m} = \mathbf{Q}(\mathbf{\Lambda} - \gamma^k \mathbf{I})^{-1} \mathbf{Q}^T \mathbf{B}^k, \quad (25)$$

where \mathbf{Q} is an orthogonal matrix composed of the eigenvectors of \mathbf{K} , $\mathbf{\Lambda}$ is a diagonal matrix containing the corresponding eigenvalues of \mathbf{K} , and γ^k is the Lagrange multiplier for the minimization of G^k . The Lagrange multiplier is calculated from the following equation, which reduces to a 6th order polynomial:

$$\mathbf{b}^T \mathbf{Q}(\mathbf{\Lambda} - \gamma^k \mathbf{I})^{-2} \mathbf{Q}^T \mathbf{b} = 1. \quad (26)$$

The matrix inversions required in (25) and (26) have simple analytical solutions since the matrices are diagonal.

Macroscopic material behavior is calculated as the expected value of the response due to the magnetic domain orientations \mathbf{m}^k . A Boltzmann distribution is used as the probability density function so that lower energy directions are favored. Thus, the strain tensor \mathbf{S} is given by the sum of the elastic and magnetoelastic strains,

$$\mathbf{S} = \mathbf{sT} + \sum_{k=1}^r \xi_{an}^k \bar{\boldsymbol{\lambda}}^k, \quad (27)$$

where \mathbf{s} is the compliance matrix for Galfenol, $\bar{\boldsymbol{\lambda}}^k$ represents the magnetostriction due to the k^{th} minimum energy direction,

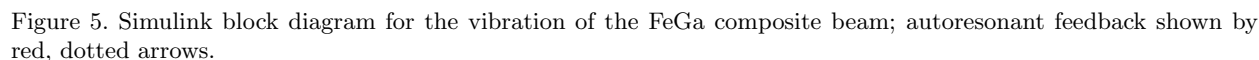
$$\bar{\boldsymbol{\lambda}}^k = \frac{3}{2} [\lambda_{100}^k m_1^2 \quad \lambda_{100}^k m_2^2 \quad \lambda_{100}^k m_3^2 \quad 2\lambda_{111}^k m_1 m_2 \quad 2\lambda_{111}^k m_2 m_3 \quad 2\lambda_{111}^k m_3 m_1]^T, \quad (28)$$

and ξ_{an}^k denotes the anhysteretic volume fraction, which is calculated as the probability of magnetic domains that are oriented along the k^{th} minimum energy direction,

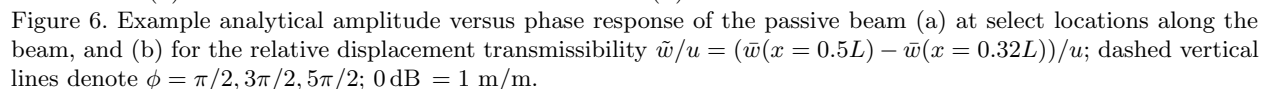
$$\xi_{an}^k = \exp\left(-\frac{G^k}{\Omega}\right) \sum_{j=1}^r \exp\left(\frac{G^j}{\Omega}\right). \quad (29)$$

where Ω is a smoothing constant. The 1-D simplification of the ED model reported by Tari et al.²³ is utilized in this work. Material constants for Galfenol used in this paper are: $K = 27.1$ kJ/m³, $K_0 = 0.021$ kJ/m³, $\mu_o M_s = 1.4889$ T, $\lambda_{100} = 156.56 \times 10^{-6}$, and $\Omega = 776.73$ J/m³ (λ_{111} is not applicable for the 1-D formulation).

A Simulink block diagram of the dynamic beam model is shown in Figure 5, where the red, dotted arrows denote the autoresonant feedback. Arbitrary, nonzero initial conditions can be used. Stability of the feedback control is ensured for most systems by limiting the magnitude of the feedback signal.¹¹ The amplitude of the resonant vibration is controlled by varying the limit. To consider the excitation magnitude's effect on the resonance tunability of the beam, Scheidler and Dapino⁹ varied the base excitation power. With autoresonant feedback, the *in situ* excitation power cannot be correctly limited. Thus, this work limits the base acceleration magnitude. As a result, f_{eq} approximately becomes a square wave.



The damping capacity for viscoelastic material damping depends on frequency.²⁴ As a result, the resonant frequency and autoresonant phase shift ϕ^* will depend on the level of damping. In this paper, the damping matrix $^n[C]$ varies temporally due to the flexural rigidity's nonuniformity, which implies that ϕ^* is time-dependent. However, as shown in the following section, the composite beam is a high Q-factor (low damping) system, for which $\omega_r \approx \omega_n$. Thus, the time dependence is neglected. For convenience, this paper uses an autoresonant feedback control with phase shift $\phi = \pm\pi/2$ (velocity feedback).



A multi-degree-of-freedom system has a set of amplitude versus phase relations, because the mass(es) on which the force is applied (loading point(s)) and on which the vibration is measured (the observation point(s)) can be selected arbitrarily and independently. For base excitation (4), the loading points are fixed. The observation point is selected by considering a passive, damped beam (i.e., uniform flexural rigidity and no axial force), for which the analytical frequency response of the displacement transmissibility (\bar{w}/u) is

given by (48) and (49) in Appendix B. A representative amplitude versus phase response at 4 locations along the symmetric beam is shown in Figure 6a. The 3 peaks in the responses correspond to the 1st, 3rd, and 5th modes of vibration, because the base excitation (4) cannot excite asymmetric modes in a clamped-clamped (symmetric) beam. The amplitude versus phase curves are not single-valued and have maxima that deviate significantly from the assumption $\phi^* = \pm\pi/2$. By observing the relative displacement between two points having opposite polarity for the 3rd and 5th modes, the amplitude versus phase curve has peaks at $\phi \approx \pi/2, 3\pi/2, 5\pi/2$ (Figure 6b). Consequently, the simplified autoresonant feedback implemented in this paper (velocity feedback) provides an accurate calculation of the resonant frequencies, as detailed in Section 3. The remaining multi-valuedness is resolved by utilizing a bandpass filter which, when tuned properly, serves as a mode selector. This bandpass filter must be carefully designed for a given system based on mode separation and amplitude versus phase characteristic response.

3. MODEL VALIDATION

Model validation is performed in two stages. First, the model is validated for a passive beam, for which an analytical solution is derived in Appendix B. Second, the model is validated for the clamped-clamped active beam by comparing measured and calculated mode shapes and resonant frequencies after calculating the Kelvin-Voigt damping constant a .

Validation of the model for a passive beam is performed by calculating the frequency response of the displacement transmissibility assuming $a = 1 \times 10^{-6}$ s. The percent error between simulated and analytical responses is shown in Figure 7, where two discretizations (h-refinement, increasing N) and two orders of differentiation accuracy (p-refinement, increasing n) are compared. The calculated response converges to the analytical using h- and p-refinement.

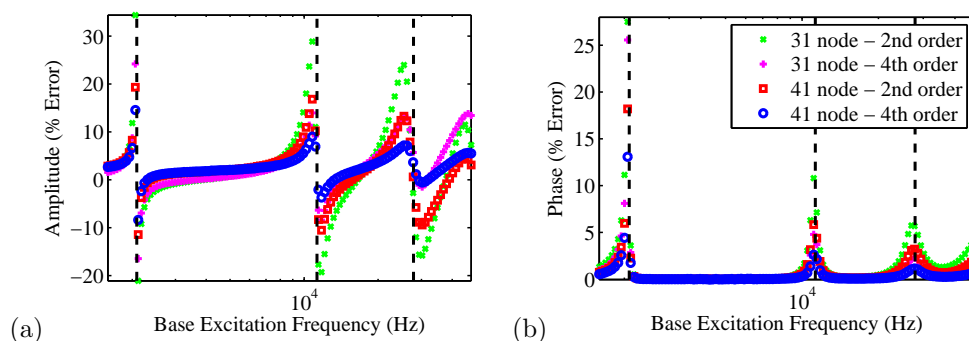


Figure 7. Calculated frequency response of the displacement transmissibility of the passive beam $\tilde{w}/u = (w(x = 0.5L) - w(x = 0.32L))/u$ compared to the analytical response (49): percent errors in the (a) amplitude and (b) phase responses; dashed vertical lines denote 1st, 3rd, and 5th undamped natural frequencies.

The autoresonant feedback control is validated by calculating the beam's vibration while discretely varying EI , and therefore ω_r . An example spectrogram of the time domain response and $\omega_r(t)$ are given in Figure 8. From an interpolated spectrogram, the resonant frequency is taken as the dominant frequency of vibration after the feedback control stabilizes. For each flexural rigidity, the analytical resonant frequencies of the 1st, 3rd, and 5th modes were calculated from (49) in Appendix B. Two metrics are used to characterize the resonant frequency tuning of the AVA (Galfenol beam): the absolute resonant frequencies and the shifts in resonant frequencies. The relative numerical error for the absolute and shift metrics are denoted by Er_A and Er_S , respectively. These errors are summarized in Table 1, where h- and p-refinement is compared. Modes 1 and 5 were distinguished using a bandpass filter. Thus, the error caused by the filter's frequency-dependent phase is included. For the passive beam, the autoresonant feedback control has a fast response time, results in vibration having a very stable frequency content, and is very accurate, with errors below 4 % for all but the 5th mode of one case.

Prior to validating the model for the active beam, the Kelvin-Voigt damping constant a was estimated from an impulse response of the clamped-clamped UAM composite that is shown in Figure 3. The damping ratio ζ_1 was calculated as 0.00217 using the logarithmic decrement method, which is applicable due to the presence of significant mode separation.²⁴ From (42), the damping constant is calculated as $a = (2\zeta_1)/\omega_1 = 3.56 \times 10^{-7}$. Transverse vibration of the UAM beam was measured using a Polytec PSV-400 scanning laser vibrometer. A periodic chirp excitation was used, because it has a nearly constant acceleration magnitude over the chirp bandwidth. The experimental setup is shown in Figure 9a. Masses were glued to the beam at the antinodes of the 3rd mode to shift the 1st and 3rd resonant frequencies into the bandwidth of the shaker. The 5th mode could not be excited. In the model, the masses were incorporated at nodes over which they were located by locally increasing ρA , such that the total mass added to the beam remained constant under h-refinement.

Figure 9b compares the measured and simulated 1st and 3rd mode shapes for a base acceleration magnitude of ~ 2 g. Since only modes 1 and 3 were considered, a bandpass filter was not needed. The laser vibrometer measurements showed that torsional motion of the masses was small compared to the transverse deflection. Experimental and calculated resonant frequencies are compared in Table 2. Discrepancies between the two can be attributed to the presence and finite size of the masses, which cause a significant increase in the beam's rotary inertia and a constraint on its local curvature. These physics are not incorporated into the model. The effect of the rotary inertia of the masses is more pronounced for the 1st mode, because displacements are an order of magnitude higher and the two outside masses rotate. Additional error may have been introduced from imperfect boundary conditions and placement of masses, and by assuming an autoresonant phase $\phi^* = \pm\pi/2$. However, considering the model's assumptions and the size of the masses relative to the beam, the accuracy is good overall.

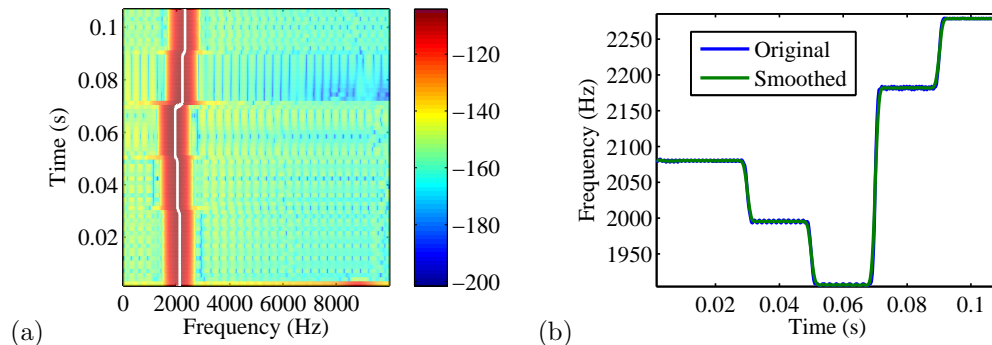


Figure 8. Tracking of the passive beam's 1st resonant frequency using autoresonant feedback control: (a) spectrogram of the simulated relative displacement \tilde{w} and (b) dominant vibration frequency versus time (overlayed in (a) as a white line); EI decreased at 0.03 and 0.05 s, and increased at 0.07 and 0.09 s.

Table 1. Autoresonant tracking of the passive beam's resonant frequency: relative numerical errors for the absolute resonant frequencies (Er_A) and shifts in resonant frequencies (Er_S).

	Mode 1		Mode 3		Mode 5	
	Er_A (%)	Er_S (%)	Er_A (%)	Er_S (%)	Er_A (%)	Er_S (%)
N=31, n=2	0.515	0.768	1.92	1.70	3.54	7.51
N=31, n=4	0.413	0.719	1.02	2.11	2.28	3.79
N=41, n=2	0.334	0.612	1.13	2.04	1.58	2.70
N=41, n=4	0.256	0.519	0.629	2.37	0.256	2.82

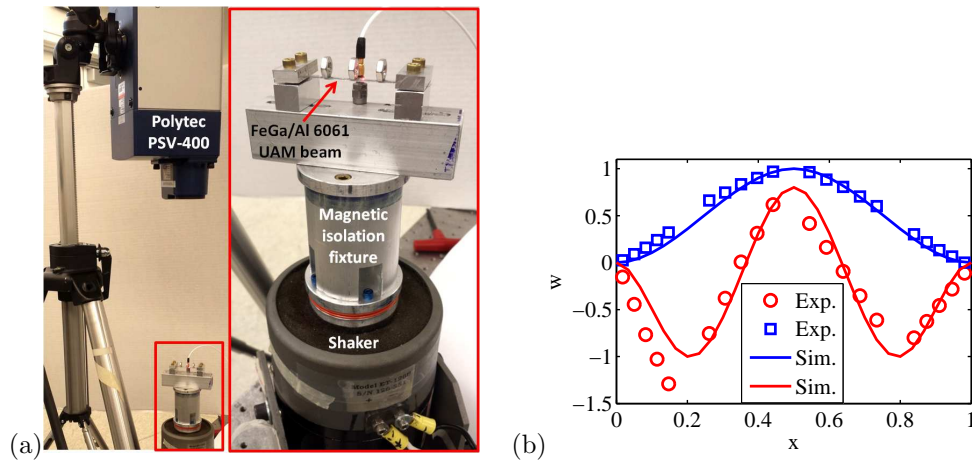


Figure 9. (a) Experimental setup for the model validation, and (b) experimental and simulated mode shapes of the UAM Galfenol/Al 6061 composite for the 1st and 3rd modes.

Table 2. Percent difference between measured and calculated resonant frequencies of the UAM Galfenol/Al 6061 beam as a function of the number of nodes N and the order of accuracy n for the approximation of spatial derivatives; experimental resonant frequencies: $\omega_{r1} = 502$ Hz, $\omega_{r3} = 2300$ Hz; $H = 0$ kA/m, $|\ddot{u}| \approx 2$ g.

	Mode 1		Mode 3	
	ω_{r1} (Hz)	Percent Difference	ω_{r3} (Hz)	Percent Difference
N=31, n=2	594	18.3	2340	1.74
N=31, n=4	598	19.1	2360	2.61
N=41, n=2	597	18.9	2310	0.43
N=41, n=4	593	18.1	2320	0.87

4. RESULTS AND DISCUSSION

To characterize the ability of the UAM Galfenol/Al 6061 beam to operate as an AVA, the resonant frequencies of the 1st and 3rd modes were calculated as a function of DC magnetic field (0–10 kA/m), base acceleration magnitude (0.5–20 g), and Galfenol volume fraction (10–100 %). Time domain responses were calculated using the Simulink model in Figure 5, but without the bandpass filter. Resonant frequencies were calculated as detailed above after the autoresonant feedback control stabilized following a change in the inputs. For each Galfenol volume fraction, the resonant frequencies were normalized by the maximum frequency to show the percent change that can be achieved by varying the DC magnetic field. This normalization is consistent with prior work,^{4,9} but is different from that used to calculate the elastic modulus changes summarized in Section 1. Results are presented as a series of surfaces (one for each Galfenol volume fraction) using the DC magnetic field and base acceleration limit as independent variables. The data are interpolated to smooth the surfaces. A top view of the surfaces is shown in Figure 10 for the 3rd mode. Results for the 1st mode are similar and are therefore not shown. For Galfenol volume fractions of 82 % and 100 %, the surfaces are less smooth, because the autoresonant feedback control had difficulty in reaching a steady state. This can be attributed to the large spatial and fast temporal variations in the composite's flexural rigidity that occur for these cases.

In all cases, the minimum resonant frequency occurs for small excitation magnitudes and weak magnetic fields, because the flexural rigidity is a minimum when stress and magnetic field are small. Weak excitations therefore allow for the greatest change in resonant frequency, because Galfenol can be easily tuned to its stiff (magnetically-saturated) state by applying stronger DC magnetic fields. As the base acceleration increases, the resulting higher stresses begin to saturate the Galfenol element. Consequently, the composite beam begins to lose its resonant frequency tunability as the Galfenol element behaves more like a passive material. These results are supported by the authors' previous work.⁹ The range of acceleration magnitudes over

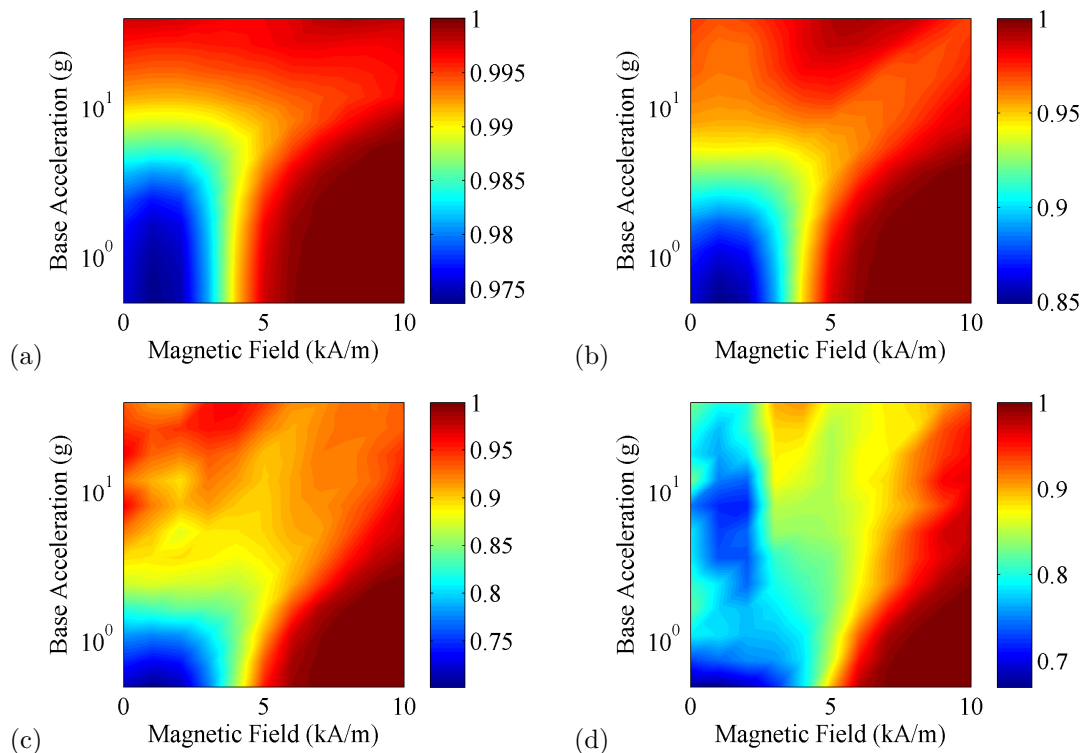


Figure 10. Normalized resonant frequency of the 3rd bending vibration mode of the clamped-clamped UAM composite as a function of the base acceleration limit and the DC magnetic field for Galfenol volume fractions of (a) 10 %, (b) 46 %, (c) 82 %, and (d) 100 %; results for 28 % and 64 % are not shown for brevity.

which the beam's behavior transitions from active to nearly passive will depend on the beam's geometry, the mass loading, and the stiffness of the matrix material. The effect of variations in Galfenol's elastic modulus on the composite's behavior will be more pronounced for composites with softer matrices (see (20)). Al 6061 is about 15 % to 130 % stiffer than Galfenol depending on stress and magnetic field. Thus, in Figure 10, the transition shifts toward smaller accelerations as Galfenol volume fraction increases.

The compressive axial force on the beam that develops in response to applied magnetic fields tends to soften the beam and reduce its resonant frequencies. This counteracts the stiffening that occurs as the magnetic field tries to saturate the Galfenol element. This is seen in Figure 10 as a broadening of the tunable region along the magnetic field axis. A broadening along the base acceleration axis was also found for high Galfenol volume fractions. This may be an artifact of the autoresonant feedback control caused by its difficulty in reaching a steady state as mentioned above. In future work, the autoresonant feedback control will be better tuned to more accurately investigate this behavior.

A figure of merit for an AVA is its maximum change in resonant frequency. The dependence of this figure of merit on Galfenol volume fraction is detailed in Figure 11 for the 1st and 3rd modes. The maximum tunability increases monotonically from 3 to 51 % as Galfenol volume fraction increases from 10 % to 100 %, respectively. The results for the 1st mode are very similar to prior work,⁹ which used a single-degree-of-freedom model and neglected the axial force. Thus, the incorporation of the axial force in this model appears to have only a small effect on the maximum tunability of the 1st resonant frequency. The maximum tunability of the 1st and 3rd resonant frequencies was found to be nearly equal except at high Galfenol volume fractions. Thus, with regard to this figure of merit, the performance of the Galfenol beam as an AVA does not degrade when operated at higher modes.

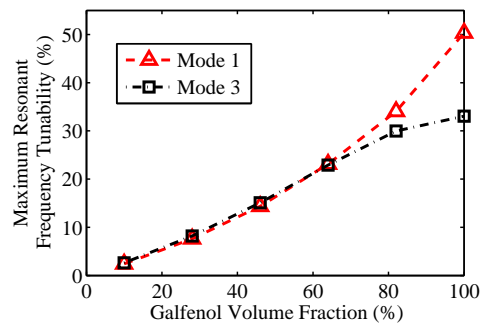


Figure 11. Maximum resonance tunability of the Galfenol/Al 6061 beam as a function of Galfenol volume fraction.

5. SUMMARY AND CONCLUSIONS

This paper investigated the use of Galfenol (FeGa) composite beams as solid-state, adaptive vibration absorbers that operate at an arbitrary vibration mode. The manufacture of these structures by ultrasonic additive manufacturing (UAM) was discussed. To characterize the stiffness tunability of the beams, a distributed parameter model of their transverse vibration was presented. The model adopts Euler-Bernoulli beam theory and incorporates Galfenol's nonlinear constitutive behavior, an axial force, viscoelastic material damping, and the beams' nonuniformity. The model was used to calculate the 1st and 3rd resonant frequencies of a FeGa/Al 6061 composite beam as a function of base acceleration, FeGa volume fraction, and DC magnetic field. Autoresonant feedback control was used as a numerical technique to maintain the resonant state under changes to the system. An extensive validation of the model was conducted using analytical responses and measurements of a FeGa/Al 6061 composite beam, which was manufactured using UAM. Additional measurements should be obtained in future work to quantify the model's performance at nonzero DC magnetic fields.

The conclusions from the study are summarized as follows:

- Autoresonant feedback control is an efficient numerical technique for the calculation of the resonant frequency of complex nonlinear systems that are subjected to changes in system parameters. For multi-degree-of-freedom systems, the performance of the control system is improved through careful selection of the vibration observation point(s) and careful tuning of the mode selector (bandpass filter).
- The composite's stiffness can be modulated between its soft and stiff states with weak DC magnetic fields of 10 kA/m or less.
- The maximum tunability of the beam's resonant frequency is possible when the base acceleration, and therefore stress in the Galfenol element, is small. A maximum tunability of 3 to 51 % was found for the UAM Galfenol/Al 6061 composites containing 10 % to 100 % Galfenol by volume, respectively.
- The axial force developed in the clamped-clamped composite due to the application of a DC magnetic field was found to have a minimal effect on the maximum resonant frequency tunability, but an appreciable effect on the range of parameters over which tuning can occur.
- With respect to the maximum resonant frequency tunability, the Galfenol beam's performance as an adaptive vibration absorber does not degrade (for most cases) when it is operated at higher modes.
- The effect of variations in Galfenol's elastic modulus on the composite's resonant frequency will be more pronounced for composites having softer matrices.

ACKNOWLEDGMENTS

This work of J.J.S. was supported by a NASA ASP fellowship and a DOE GATE fellowship from the U.S. DOE GATE Center of Excellence, DE FG2605NT42616, at The Ohio State University. Additional support was provided by the member organizations of the Smart Vehicle Concepts Center (www.SmartVehicleCenter.org), a National Science Foundation Industry/University Cooperative Research Center (I/UCRC).

REFERENCES

- [1] Brennan, M., "Some recent developments in adaptive tuned vibration absorbers/neutralisers," *Shock and Vibration* **13**(4), 531–543 (2006).
- [2] Bein, T., Bös, J., Herold, S., Mayer, D., Melz, T., and Thomaier, M., "Smart interfaces and semi-active vibration absorber for noise reduction in vehicle structures," *Aerospace Science and Technology* **12**(1), 62–73 (2008).
- [3] Atulasimha, J. and Flatau, A., "A review of magnetostrictive iron–gallium alloys," *Smart Materials and Structures* **20**(4), 043001 (2011).
- [4] Datta, S., Atulasimha, J., Mudivarthi, C., and Flatau, A., "Stress and magnetic field-dependent Young's modulus in single crystal iron–gallium alloys," *Journal of Magnetism and Magnetic Materials* **322**(15), 2135–2144 (2010).
- [5] Clark, A. and Savage, H., "Giant magnetically induced changes in the elastic moduli in Tb_{0.3}Dy_{0.7}Fe₂," *IEEE Transactions on Sonics and Ultrasonics* **22**(50) (1975).
- [6] CTS Corp., "PZT5A and 5H data sheet," available online (2014).
- [7] Clark, W., "Vibration control with state-switched piezoelectric materials," *Journal of intelligent material systems and structures* **11**(4), 263–271 (2000).
- [8] Scheidler, J. and Dapino, M., "Nonlinear dynamic model for magnetically-tunable Galfenol vibration absorbers," in *[Proceedings of SPIE]*, **8690**, **869002** (2013).
- [9] Scheidler, J. and Dapino, M., "Nonlinear dynamic modeling and resonance tuning of Galfenol vibration absorbers," *Smart Materials and Structures* **22**(8), 085015 (2013).
- [10] Babitsky, V., "Autoresonant mechatronic systems," *Mechatronics* **5**(5), 483–495 (1995).
- [11] Sokolov, I. and Babitsky, V., "Phase control of self-sustained vibration," *Journal of sound and vibration* **248**(4), 725–744 (2001).
- [12] Voronina, S. and Babitsky, V., "Autoresonant control strategies of loaded ultrasonic transducer for machining applications," *Journal of Sound and Vibration* **313**(3–5), 395–417 (2008).
- [13] Twiefel, J., "Vibration shape effects on the power output in piezoelectric vibro-impact energy harvesters," in *[Proceedings of SPIE]*, **8688**, **86880K** (2013).
- [14] Evans, P. and Dapino, M., "Efficient magnetic hysteresis model for field and stress application in magnetostrictive Galfenol," *Journal of Applied Physics* **107**(6), 063906 (2010).
- [15] Shu, L., Headings, L., Dapino, M., Chen, D., and Lu, Q., "Nonlinear model for galfenol cantilevered unimorphs considering full magnetoelastic coupling," *Journal of Intelligent Material Systems and Structures* **25**(2), 187–203 (2013).
- [16] Meirovitch, L., *[Fundamentals of Vibrations]*, Waveland Press, Inc., Long Grove, IL, 1 ed. (2010).
- [17] Hoffmann, K. A. and Chiang, S. T., *[Computational fluid dynamics]*, Engineering Education System, Wichita, KS (2000).
- [18] Agarwal, B., Broutman, L., and Chandrashekhara, K., *[Analysis and performance of fiber composites]*, John Wiley & Sons, Inc., Hoboken, NJ, 3 ed. (2006).
- [19] Chakrabarti, S. and Dapino, M., "Nonlinear finite element model for 3D Galfenol systems," *Smart Materials and Structures* **20**(10), 105034 (2011).
- [20] Evans, P. and Dapino, M., "Dynamic model for 3-D magnetostrictive transducers," *IEEE Transactions on Magnetics* **47**(1), 221–230 (2011).
- [21] Weng, L., Walker, T., Deng, Z., Dapino, M., and Wang, B., "Major and minor stress-magnetization loops in textured polycrystalline Fe_{81.6}Ga_{18.4} Galfenol," *Journal of Applied Physics* **113**(2), 024508 (2013).
- [22] Chakrabarti, S., *Modeling of 3D magnetostrictive systems with application to Galfenol and Terfenol-D transducers*, PhD thesis, The Ohio State University (2011).
- [23] Tari, H., Scheidler, J., and Dapino, M., "Robust solution procedure for the discrete energy-averaged model on calculation of the 3D hysteretic magnetization and magnetostriction of iron-gallium alloys," *Journal of Applied Physics* (In review).
- [24] De Silva, C., *[Vibration: Fundamentals and Practice]*, CRC Press, Boca Raton, FL, 2 ed. (2006).
- [25] Rao, S., *[Mechanical Vibrations]*, Pearson Prentice Hall, Upper Saddle River, NJ, 4 ed. (2003).

APPENDIX A. STIFFNESS AND DAMPING MATRICES

For the 2nd order central difference approximation of the damping and flexural forces ((8) and (9)), the global damping and stiffness matrices are, respectively,

$$[C] = a(\Delta x)^{-4} \begin{bmatrix} C_2 + G_2 & B_2 & A_2 & 0 & \cdots & \cdots & 0 \\ D_3 & C_3 & B_3 & A_3 & 0 & \cdots & \\ G_4 & D_4 & C_4 & B_4 & A_4 & 0 & \vdots \\ 0 & \ddots & \ddots & \ddots & \ddots & \ddots & 0 \\ \vdots & 0 & G_{N-3} & D_{N-3} & C_{N-3} & B_{N-3} & A_{N-3} \\ \cdots & \cdots & 0 & G_{N-2} & D_{N-2} & C_{N-2} & B_{N-2} \\ 0 & \cdots & \cdots & 0 & G_{N-1} & D_{N-1} & C_{N-1} + A_{N-1} \end{bmatrix}, \quad (30)$$

and

$$[K] = (\Delta x)^{-4} \begin{bmatrix} \bar{C}_2 + G_2 & \bar{B}_2 & A_2 & 0 & \cdots & \cdots & 0 \\ \bar{D}_3 & \bar{C}_3 & \bar{B}_3 & A_3 & 0 & \cdots & \\ G_4 & \bar{D}_4 & \bar{C}_4 & \bar{B}_4 & A_4 & 0 & \vdots \\ 0 & \ddots & \ddots & \ddots & \ddots & \ddots & 0 \\ \vdots & 0 & G_{N-3} & \bar{D}_{N-3} & \bar{C}_{N-3} & \bar{B}_{N-3} & A_{N-3} \\ \cdots & \cdots & 0 & G_{N-2} & \bar{D}_{N-2} & \bar{C}_{N-2} & \bar{B}_{N-2} \\ 0 & \cdots & \cdots & 0 & G_{N-1} & \bar{D}_{N-1} & \bar{C}_{N-1} + A_{N-1} \end{bmatrix}, \quad (31)$$

where the elements are evaluated using (10).

For increased accuracy, the 4th order central difference method can be used to approximate the damping and flexural forces as

$$F_i^C(t) \approx a(144\Delta x)^{-4} (H_i \dot{w}_{i+3} + J_i \dot{w}_{i+2} + L_i \dot{w}_{i+1} + N_i \dot{w}_i + O_i \dot{w}_{i-1} + Q_i \dot{w}_{i-2} + R_i \dot{w}_{i-3}), \quad (32)$$

and

$$\begin{aligned} F_i^K(t) &\approx (144\Delta x)^{-4} (H_i \dot{w}_{i+3} + (J_i + 12\bar{P}) \dot{w}_{i+2} + (L_i - 192\bar{P}) \dot{w}_{i+1} \\ &\quad + (N_i + 360\bar{P}) \dot{w}_i + (O_i - 192\bar{P}) \dot{w}_{i-1} + (Q_i + 12\bar{P}) \dot{w}_{i-2} + R_i \dot{w}_{i-3}) \\ &= (144\Delta x)^{-4} (H_i \dot{w}_{i+3} + \bar{J}_i \dot{w}_{i+2} + \bar{L}_i \dot{w}_{i+1} + \bar{N}_i \dot{w}_i + \bar{O}_i \dot{w}_{i-1} + \bar{Q}_i \dot{w}_{i-2} + R_i \dot{w}_{i-3}) \end{aligned} \quad (33)$$

where

$$\begin{aligned} H_i &= 3EI_{i+2} - 24EI_{i+1} - 24EI_i + 24EI_{i-1} - 3EI_{i-2} \\ J_i &= -23EI_{i+2} + 176EI_{i+1} + 318EI_i - 208EI_{i-1} + 25EI_{i-2} \\ L_i &= 23EI_{i+2} - 56EI_{i+1} - 1416EI_i + 568EI_{i-1} - 55EI_{i-2} \\ N_i &= 30EI_{i+2} - 480EI_{i+1} + 2244EI_i - 480EI_{i-1} + 30EI_{i-2} \\ O_i &= -55EI_{i+2} + 568EI_{i+1} - 1416EI_i - 56EI_{i-1} + 23EI_{i-2} \\ Q_i &= 25EI_{i+2} - 208EI_{i+1} + 318EI_i + 176EI_{i-1} - 23EI_{i-2} \\ R_i &= -3EI_{i+2} + 24EI_{i+1} - 24EI_i - 24EI_{i-1} + 3EI_{i-2} \end{aligned} \quad (34)$$

Using (32) - (34), the 4th order accurate damping and stiffness matrices can be written as

$$[C] = a(144\Delta x)^{-4} \begin{bmatrix} \tau(C_2 + G_2) & \tau B_2 & \tau A_2 & 0 & \cdots & & & & 0 \\ O_3 + R_3 & N_3 & L_3 & J_3 & H_3 & 0 & \cdots & & \\ Q_4 & O_4 & N_4 & L_4 & J_4 & H_4 & 0 & \cdots & \\ R_5 & Q_5 & O_5 & N_5 & L_5 & J_5 & H_5 & 0 & \vdots \\ 0 & \ddots & \ddots & \ddots & \ddots & \ddots & \ddots & \ddots & 0 \\ \vdots & 0 & R_{N-4} & Q_{N-4} & O_{N-4} & N_{N-4} & L_{N-4} & J_{N-4} & H_{N-4} \\ & \cdots & 0 & R_{N-3} & Q_{N-3} & O_{N-3} & N_{N-3} & L_{N-3} & J_{N-3} \\ & & \cdots & 0 & R_{N-2} & Q_{N-2} & O_{N-2} & N_{N-2} & L_{N-2} + H_{N-2} \\ 0 & & & \cdots & 0 & \tau G_{N-1} & \tau D_{N-1} & \tau(C_{N-1} + A_{N-1}) \end{bmatrix}, \quad (35)$$

and

$$[K] = (144\Delta x)^{-4} \begin{bmatrix} \tau(\bar{C}_2 + G_2) & \tau \bar{B}_2 & \tau A_2 & 0 & \cdots & & & & 0 \\ \bar{O}_3 + R_3 & \bar{N}_3 & \bar{L}_3 & \bar{J}_3 & \bar{H}_3 & 0 & \cdots & & \\ \bar{Q}_4 & \bar{O}_4 & \bar{N}_4 & \bar{L}_4 & \bar{J}_4 & \bar{H}_4 & 0 & \cdots & \\ R_5 & \bar{Q}_5 & \bar{O}_5 & \bar{N}_5 & \bar{L}_5 & \bar{J}_5 & \bar{H}_5 & 0 & \vdots \\ 0 & \ddots & \ddots & \ddots & \ddots & \ddots & \ddots & \ddots & 0 \\ \vdots & 0 & R_{N-4} & \bar{Q}_{N-4} & \bar{O}_{N-4} & \bar{N}_{N-4} & \bar{L}_{N-4} & \bar{J}_{N-4} & \bar{H}_{N-4} \\ & \cdots & 0 & R_{N-3} & \bar{Q}_{N-3} & \bar{O}_{N-3} & \bar{N}_{N-3} & \bar{L}_{N-3} & \bar{J}_{N-3} \\ & & \cdots & 0 & R_{N-2} & \bar{Q}_{N-2} & \bar{O}_{N-2} & \bar{N}_{N-2} & \bar{L}_{N-2} + \bar{H}_{N-2} \\ 0 & & & \cdots & 0 & \tau G_{N-1} & \tau \bar{D}_{N-1} & \tau(\bar{C}_{N-1} + A_{N-1}) \end{bmatrix}, \quad (36)$$

where $\tau = 144$. Since the 4th order approximations of the damping and flexural forces at node i depend upon nodes $i - 3$ and $i + 3$, the 2nd order central difference method must be used at nodes $i = 2, N - 1$ to avoid the inclusion of fictitious nodal displacements in the 4th order damping and stiffness matrices. The 4th order method can be used at the remaining interior nodes after considering (11).

APPENDIX B. ANALYTICAL RESPONSE OF THE PASSIVE BEAM

The analytical free and forced vibration of the passive beam (i.e., uniform flexural rigidity and no axial force) are derived as follows. By the method of modal analysis, the solution for the beam vibration can be written as

$$\bar{w}(x, t) = \sum_{r=1}^{\infty} W_r(x) \eta_r(t), \quad (37)$$

where $\eta_r(t)$ are the modal coordinates and $W_r(x)$ are the eigenfunctions of the undamped clamped-clamped beam, which are provided by Rao,²⁵

$$W_r(x) = C_n \left[\sinh(\beta_r x) - \sin(\beta_r x) + \left(\frac{\sinh(\beta_r L) - \sin(\beta_r L)}{\cosh(\beta_r L) - \cos(\beta_r L)} \right) (\cosh(\beta_r x) - \cos(\beta_r x)) \right], \quad (38)$$

$$\cos(\beta_r L) \cosh(\beta_r L) = 1. \quad (39)$$

Inserting (37) into the governing PDE (3), neglecting the beam nonuniformity and axial force, premultiplying by $W_s(x)$, and integrating over the length of the beam yields

$$\sum_{r=1}^{\infty} \left(\left(\int_0^L \rho A W_s W_r dx \right) \ddot{\eta}_r + a \left(\int_0^L EI W_s W_r^{(4)} dx \right) \dot{\eta}_r + \left(\int_0^L EI W_s W_r^{(4)} dx \right) \eta_r \right) = \int_0^L W_r f_{eq} dx. \quad (40)$$

Using the orthonormality conditions¹⁶ derived from the eigenvalue problem, only the s^{th} terms in (40) survive, giving the modal equations,

$$\ddot{\eta}_s + 2\zeta_s \omega_s \dot{\eta}_s + \omega_s^2 \eta_s = \Phi_s \sin(\omega_u t), \quad s = 1, 2, \dots, \quad (41)$$

where the modal damping ratio ζ_s is

$$\zeta_s = \frac{a \omega_s}{2}. \quad (42)$$

Assuming harmonic base excitation with frequency ω_u and magnitude $B(\omega_u)$, the forcing magnitude Φ_s is

$$\Phi_s = \rho A B(\omega_u) \omega_u^2 \int_0^L W_s dx. \quad (43)$$

For underdamped modes, the solution of (41) can be written as

$$\eta_s = \exp(-\zeta_s \omega_s t) (A \sin(\omega_{ds} t) + B \cos(\omega_{ds} t)) + \Phi_s \left| \tilde{G}_s(i\omega_u) \right| \sin(\omega_u t + \phi_s), \quad (44)$$

where ω_{ds} is the damped natural frequency of the s^{th} mode, the magnitude and phase of the modal frequency response, respectively, are

$$\left| \tilde{G}_s(i\omega_u) \right| = \frac{1}{\omega_s^2} \left(\left(1 - \left(\frac{\omega_u}{\omega_s} \right)^2 \right)^2 + \left(2\zeta_s \frac{\omega_u}{\omega_s} \right)^2 \right)^{-1/2}, \quad (45)$$

$$\phi_s = -\tan^{-1} \left(2\zeta_s \frac{\omega_u}{\omega_s} \left(1 - \left(\frac{\omega_u}{\omega_s} \right)^2 \right)^{-1} \right), \quad (46)$$

and the undetermined coefficients A and B are

$$\begin{aligned} A &= \eta_s(0) - \sin(\phi_s) \Phi_s \left| \tilde{G}_s(i\omega_u) \right| \\ B &= \frac{\dot{\eta}_s(0) + \zeta_s \omega_s \eta_s(0)}{\omega_{ds}} - \frac{\zeta_s \omega_s \sin(\phi_s) + \omega_u \cos(\phi_s)}{\omega_{ds}} \Phi_s \left| \tilde{G}_s(i\omega_u) \right|. \end{aligned} \quad (47)$$

Insertion of (44) and (38) into (37) gives the time domain response of the passive beam to initial conditions and base excitation. The frequency response of the displacement transmissibility can be written as

$$\begin{aligned} G(x, i\omega_u) &= \frac{\bar{w}}{u} = \rho A \omega_u^2 \sum_{s=1}^{\infty} W_r(x) \left(\int_0^L W_s dx \right) \left| \tilde{G}_s(i\omega_u) \right| \exp(i\phi_s) \\ &= \sum_{s=1}^{\infty} \Omega_s(x, i\omega_u) \exp(i\phi_s) \end{aligned} \quad (48)$$

The magnitude and phase of $G(x, i\omega_u)$ are

$$\begin{aligned} |G(x, i\omega_u)| &= \left(\left(\sum_{s=1}^{\infty} \Omega_s(x, i\omega_u) \cos(\phi_s) \right)^2 + \left(\sum_{s=1}^{\infty} \Omega_s(x, i\omega_u) \sin(\phi_s) \right)^2 \right)^{1/2} \\ \angle G(x, i\omega_u) &= \tan^{-1} \left(\frac{\sum_{s=1}^{\infty} \Omega_s(x, i\omega_u) \sin(\phi_s)}{\sum_{s=1}^{\infty} \Omega_s(x, i\omega_u) \cos(\phi_s)} \right) \end{aligned} \quad (49)$$